ECS Advances, 2023 **2** 026503

One Pot Synthesis of CuO-$CuFe_2O_4$@rGO Nanostructure with Synergistic Effect for Efficient Electrochemical Sensing Application of Paracetamol

Jagdish C. Bhangoji,[1] Sandeep S. Kahandal,[2] Rahul S. Patil,[3] Trimurti L. Lambat,[4,z] Shirinaz I. Khan,[5] Gurumeet Wadhava,[6] Sami H. Mahmood,[7] and Suresh S. Shendage[1,z]

[1]*Department of Chemistry, Vinayak Ganesh Vaze College of Arts, Commerce and Science (Autonomous), Mithagar Road, Mulund (E), Mumbai, Maharashtra—400081, India*
[2]*Department of Chemistry, VPM's B. N. Bandodkar College of Science (Autonomous), Jnanadweepa, Chedani Bunder Road, Thane (W), Mumbai, Maharashtra—400601, India*
[3]*Department of Chemistry, Yashwantrao Chavan College of Science, Karad, Satara, Maharashtra –415105, India*
[4]*Department of Chemistry, Manoharbhai Patel College of Arts, Commerce & Science, Deori- 441901, Gondia, Maharashtra, India*
[5]*Department of Chemistry, Shankarlal Agrawal Science College, Salekasa, Gondia Maharashtra- 441916, India*
[6]*Department of Chemistry, Veer Sanskar A. C. S. College, Phunde, Panvel, Navi Mumbai (Maharashtra)—410206, India*
[7]*Department of Physics, The University of Jordan, Amman 11942, Jordan*

In the present study, the facile and synergistic approach for electrochemical sensing of paracetamol (PA) drug was demonstrated by hydrothermally synthesized copper oxide-copper ferrite nanohybrid composite supported on reduced graphene oxide (CuO-$CuFe_2O_4$@rGO) glassy carbon electrode. The surface texture and structural information of the electrode material were examined by FE-SEM, HR-TEM, and X-ray diffraction techniques, whereas the electrochemical sensing application of paracetamol oxidation was investigated by amperometric method. The average crystallite size of CuO-$CuFe_2O_4$ was calculated from XRD data and found to be 35.45 nm. The fabricated sensor exhibited a higher sensitivity of 970.26 $\mu A.mM^{-1}.cm^{-2}$ along with a lower limit of detection (LOD) and limit of quantification (LOQ) of 7.0 μM and 25 μM, respectively, with a linear dynamic range of 10–1200 μM. Furthermore, the CuO-$CuFe_2O_4$@rGO modified sensor showed excellent anti-interferents ability, long-term stability and reproducibility towards electro-oxidation of paracetamol drug. Moreover, it can be efficiently applied for the analysis of paracetamol in biological samples. Finally, the synthesized nanocomposite material was validated to be a competent electrocatalyst for electrochemical sensing application of paracetamol.
 [DOI: 10.1149/2754-2734/acd800]

Manuscript submitted February 6, 2023; revised manuscript received May 9, 2023. Published June 1, 2023.

Supplementary material for this article is available online

Drugs like paracetamol (PA) are used as both antipyretics and painkillers. It is frequently used to treat a variety of ailments, including coughing, migraines, headaches, different types of bodily aches, and menstruation discomfort. Generally speaking, it is prescribed in many nations throughout the world as an aspirin substitute.[1–4] At lesser doses, paracetamol normally has no harmful side effects since it is quickly absorbed in the stomach and completely used by the body. However, a high dosage can have a number of negative consequences, including discomfort in the pancreas, kidney and liver problems, hepatic insufficiency, skin irritation, and skin rashes.[5,6] Thus, fast, sensitive and specific determination of paracetamol is essential for further investigation.

Different analytical techniques such as, chemiluminescence,[7,8] spectrophotometry,[9] capillary electrophoresis,[10] chromatography,[11] flow-injection analysis,[12] titrimetry,[13] electroanalytical[14,15] etc., have been employed for paracetamol analysis. However, different disadvantages including high cost, lengthy analysis and complex procedures render some techniques unfavourable.[16] Accordingly, the electroanalytical method is frequently used due to its simplicity, rapid response, cost effectiveness, high accuracy, selectivity and sensitivity.[17–19]

Unlike bulk materials, nanomaterials exhibit improved catalytic performance in various applications owing to their unique structural characteristics. Specifically, nanomaterials are widely used in applications including chemical sensors and bio-sensors.[20] In the last decade, a wide variety of nanocomposite materials were widely studied as catalytic materials for paracetamol oxidation reactions. These include polyimide-multi-walled carbon nanotube (polyimide-MWCNTs),[3] AuPd/GN-CNTs-IL (GN is Graphene nanotube, CNTs is Carbon Nanotubes, and IL is Ionic Liquid),[6] MWCNTs/CTS-Cu (CTS is chitosan),[21] GO/carbon black/chitosan (GO is Graphene Oxide),[22] GO-XDA-Mn_2O_3 (XDA is Xylenediamine),[23] GC/CNT/PEDOT/NF/Crown ether (where PEDOT is poly (3–4-Ethylenedioxy Thiophene).[24] Other hybrid materials such as mesoporous chitosan/silica hybrid material,[25] rGO/carbon black/chitosan,[26] chitosan - carbon paste,[27] and MWCNT/HSA-oppy were used as electrode materials.[28] Additionally, biomolecules and polymeric materials such as poly (L-leucine),[29] cellulose and starch polymers-Co NPs,[16] nano Molecularly Imprinted Polymers (MIP),[1] MIP/PB,[30] and MIP micelle were used.[31] Moreover, noble metal-based composites such as Pd/MnO_2 NRs/graphene,[32] Pd nanoclusters/polyfuran,[33] Pd graphene oxide,[34] Pd nanorods @hollow N, S-doped C were employed.[35] However, the high cost, complex synthetic procedure and instability of biomolecules and polymers limit their applications in paracetamol detection.

Hence, to overcome these shortcomings, different transition metal oxides were investigated, and revealed fascinating properties and merits for sensing purposes including low cost, high surface-volume ratio, non-toxicity, greater conductivity and semiconducting nature, sensitivity and rapid response.[36–39] Recently, many transition metal oxides like NiO,[4] CuO,[19] MnO_2,[32] TiO_2,[20,40] ZnO,[41] and Fe_2O_3[42] with different support materials have been extensively employed for electrochemical sensing of paracetamol. Among these, magnetite (Fe_2O_3) was widely used for different applications like sensors, catalysis, solar cells, and energy renovation owing to its non-toxicity, low cost, high stability, bio-compatibility, enzyme mimetic action (peroxidase enzyme) and *n*-type semiconducting nature with a band gap of 2.0–2.2 eV suitable for visible light absorption. Additionally, it

[z]E-mail: lambatges@gmail.com; sureshsshendage@gmail.com

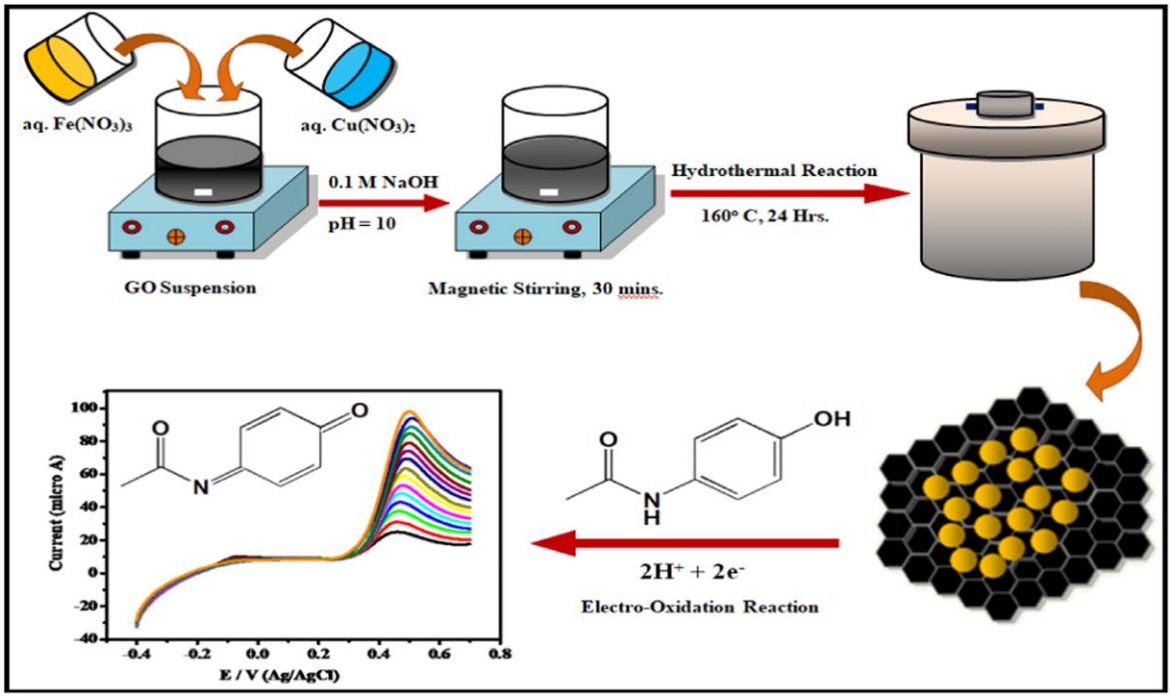

Scheme 1. Schematic representation of the synthesis and electrochemical application of CuO-$CuFe_2O_4$@rGO for PA.

shows higher oxygen ion mobility that enhances electro-catalytic performance in redox reactions.[43–45] Nevertheless, the higher electron-hole rearrangement and lower electron transport in Fe_2O_3 decrease the catalytic reaction rate which limits its electrochemical sensing capabilities.[46,47] Thus, to improve the conductivity and catalytic activity of metal oxide materials, more conducting support materials were used.[47] Specifically, combinations (nanocomposites) of carbonaceous support materials with metal oxides revealed improved characteristics for different sensing applications such superior conductivity, excellent catalytic activity, biocompatibility, easy functionalization and high active surface area.[43,48,49] In the earlier decade, numerous supporting materials were employed such as polyimide,[3] 3D graphene,[6] cellulose and starch polymers,[16] MWCNT,[21,41] chitosan,[25] polyfuran,[33] GO,[34] and carbon.[35,40] Nowadays, it was established that reduced graphene oxide (rGO) is an effective competent support for growth and dispersion of different nanomaterials because of its excellent features such as 2D structure, higher conductivity, enormous surface area, and plenty of active functional groups.[46] In addition, the higher conductivity of copper ferrite ($CuFe_2O_4$) compared to magnetite makes it a promising candidate with enhanced electro-catalytic performance.

Herein, we embarked on employing a low-cost ferrite with favourable characteristics for paracetamol detection. The work is motivated by the fact that ferrites possess (Peroxidase) enzyme mimetic action with higher content of O^{2-} ion which enhances the paracetamol oxidation compared to other metal oxides and higher-cost nanocomposite materials reported in literature. The employment of copper ferrite is motivated be the fact that it possesses a higher conductivity than magnetite, which improves the synergistic effect for electrochemical sensing. Also, coating the ferrite particles with CuO (having low band gap and large surface area) is expected to induce enhancement of the active surface area, electrical conductivity and electrochemical activity in contrast to other composite materials. The results of this work are expected to be beneficial for the pharmaceutical analysis of the paracetamol drug which may induce harmful side effects on high concentrations.

In this work, we describe a simple one-pot hydrothermal synthesis of CuO-$CuFe_2O_4$@rGO composite material without using hazardous chemical reducing or stabilizing agents. In the synthesis, NaOH was used as a reducing and precipitating agent for GO as well as metal ion under hydrothermal pressure. 2D rGO serves as an outstanding substrate material for the growth and anchoring of CuO-$CuFe_2O_4$ nanoparticles. The outer surface texture of the CuO-$CuFe_2O_4$@rGO material was studied in detail. The decoration of CuO-$CuFe_2O_4$ on of rGO support enhanced the electrical properties through the synergistic effect between the components of the hybrid material. The synthesized CuO-$CuFe_2O_4$@rGO nanocomposite revealed improved potential for the electro-oxidation of paracetamol. A schematic representation of the synthesis and amperometric detection of acetaminophen by the CuO-$CuFe_2O_4$@rGO/GCE sensor is shown in (Scheme 1), where the electro-oxidation mechanism of paracetamol is illustrated by:[63]

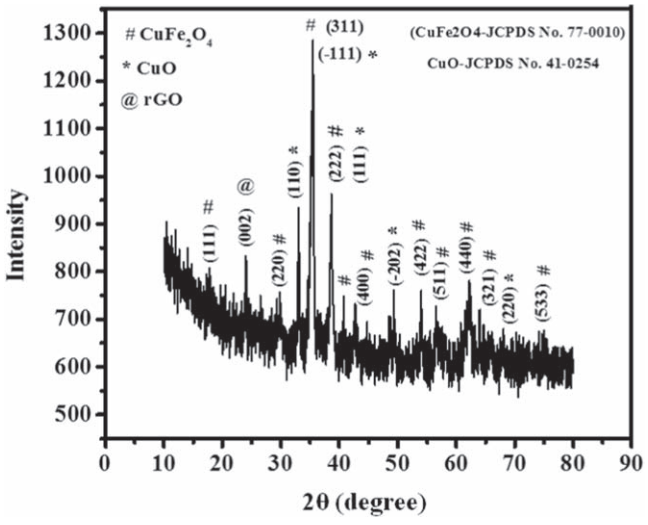

Figure 1. X-ray diffraction pattern (XRD) of CuO-$CuFe_2O_4$@rGO nanocomposite.

Experimental

Reagents and chemicals.—The chemicals used in this work consist of natural graphite powder (Molychem, LR, 98%), Sulphuric

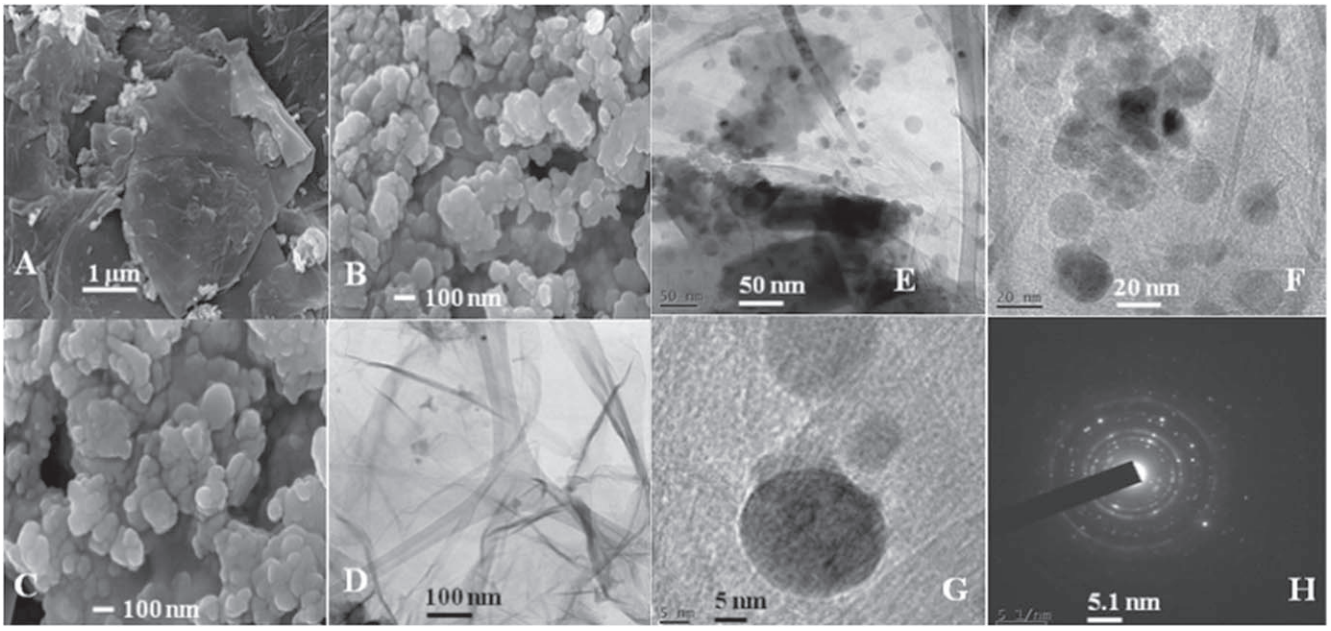

Figure 2. FE-SEM images (2 A) rGO, (2B-2C) CuO-$CuFe_2O_4$@rGO and HR-TEM images of rGO (2D), CuO-$CuFe_2O_4$@rGO (2E-2G) and SEAD pattern (2H).

acid (Molychem, AR, 98%), Phosphoric acid (Molychem, AR, 98%), $KMnO_4$ (Molychem, AR, 98%), Sodium hydroxide, Ethanol, paracetamol tablet commercially available, ascorbic acid, dopamine, uric acid, KCl, and NaCl. Other reagents and chemicals used were of high purity. Ultra-pure water was used for the preparation of sample solutions throughout experiment.

Instruments.—An electro-catalytic study was carried out with potentiostat-galvanostat DY2300 series Potentiostat electrochemical workstation (Austin, TX, USA). Three electrode cell set up was employed for electrochemical experiments. The CuO-$CuFe_2O_4$@rGO modified GCE (3 mm) was used as a working electrode, and Pt foil counter and Ag/AgCl reference, respectively. The morphological examination was done using high-resolution transmission electron microscope (HR-TEM) operating at 10 kV and field emission scanning electron microscope (FE-SEM, JSM-7600F) operating at 10 kV. X-ray diffraction (XRD) analysis was carried out using a Panalytical, Netherlands instrument with Cu-K_α radiation and Operating potential of 45 kV. Magnetic stirrer (REMI, 1MLH) and a Centrifuge were used in the synthesis.

Synthesis methods.— *Synthesis of graphene oxide (GO).*—The precursor graphite oxide (GO) was prepared via exfoliation of natural graphite powder by using previously reported modified Hummer's process.[50,51] In the typical synthesis procedure, 2.5 g of graphite powder and 1.25 g of $NaNO_3$ were carefully dissolved in an acid mixture of (H_2SO_4 + H_3PO_4) with constant stirring. After 10 min, 8 g of $KMnO_4$ was slowly added to the mixture with constant stirring a temperature under 5 °C in an ice bath to avoid extra heating and explosion. The resulting reaction mixture was then vigorously stirred at 35 °C for 12 h to complete oxidation and exfoliation reaction. Then, 200 ml of distilled water was added to intermediate product. To this, 8 ml H_2O_2 was added for the completion of oxidation of graphite to graphene oxide (GO). At last, the product was filtered using a centrifuge at 10,000 rpm and washed several times with dilute HCl. Finally, the obtained GO product was desiccated at 60 °C in an oven.

CuO-$CuFe_2O_4$@rGO nanocomposite preparation.—The CuO-$CuFe_2O_4$@rGO nanocomposite was synthesized by a facile hydrothermal route. In the process, 100 mg GO was finely diffused into 50 ml D/W through sonication for 1 h (solution-A). Afterwards, the stoichiometric amount of $Cu(NO_3)_2.3H_2O$ and $Fe(NO_3)_3.9H_2O$ were dissolved in 25 ml of distilled water with constant stirring for 20 min (solution-B). Subsequently, solution-B was transferred into solution A, followed by vigorous mixing for 30 min for homogenisation purposes. After that, pH of the reaction precursor was adjusted at 10 by adding 0.1 M sodium hydroxide solution dropwise. Subsequently, the reaction mixture was alternately stirred and sonicated for 20 min (3 times). Afterwards, the reaction mixture was transferred into a 150 ml Teflon-coating steel autoclave and kept in an oven at 160 °C for 24 h. After this stage, the mixture was naturally cooled to room temperature. The product was then separated by centrifuging followed by washing with distilled water several times as well as alcohol. Finally, the product was dried in an oven at 70 °C. The CuO-$CuFe_2O_4$ was synthesized through similar method and used for comparison.

Fabrication of CuO-$CuFe_2O_4$@rGO/GCE modified electrode.—Prior to fabrication of the electrode, a bare glassy carbon electrode was cleaned by rubbing on 0.05, 0.3 μm alumina powder-water paste. Then, the bare electrode was rinsed by ultra-sonication in ethanol and distilled water for 10 min, respectively, to remove any impurity. The ink of CuO-$CuFe_2O_4$@rGO nanocomposite was prepared by dissolving in ethanol solvent (1 mg ml^{-1}) via ultra-sonication for 30 min. To modify GCE, 10 μl of the composite ink was dropped on ultra-clean surface of GCE followed by air drying. Other electrodes including $CuFe_2O_4$@GCE, rGO@GCE were fabricated through similar process and used for comparison purpose.

Results and Discussion

Structural and morphological characterization.—The X-ray diffraction analysis was used to examine the structural characteristics of the nanomaterials. (Fig. 1) shows the X-ray diffraction pattern (XRD) of CuO-$CuFe_2O_4$@rGO nanocomposite. The characteristic diffraction peaks observed at the angular positions 2θ = 18.1°, 30.1°, 35.5°, 37.6°, 43.2°, 53.7°, 57.1°, 62.7°, 64.1° and 74.6° correspond to the (111), (220), (311), (222), (400), (422), (511), (440), (321) and (533) crystal planes of the cubic copper ferrite, and indicate that this phase is polycrystalline in nature. The observed reflections are consistent with the standard diffraction pattern of $CuFe_2O_4$ (JCPDS file no. 77-0010).[52–55] In addition, the single diffraction peak at $2\theta = 23.8°$ corresponds to the (002) plane of rGO sheets,[56,57] which indicates a single crystal structure which is highly

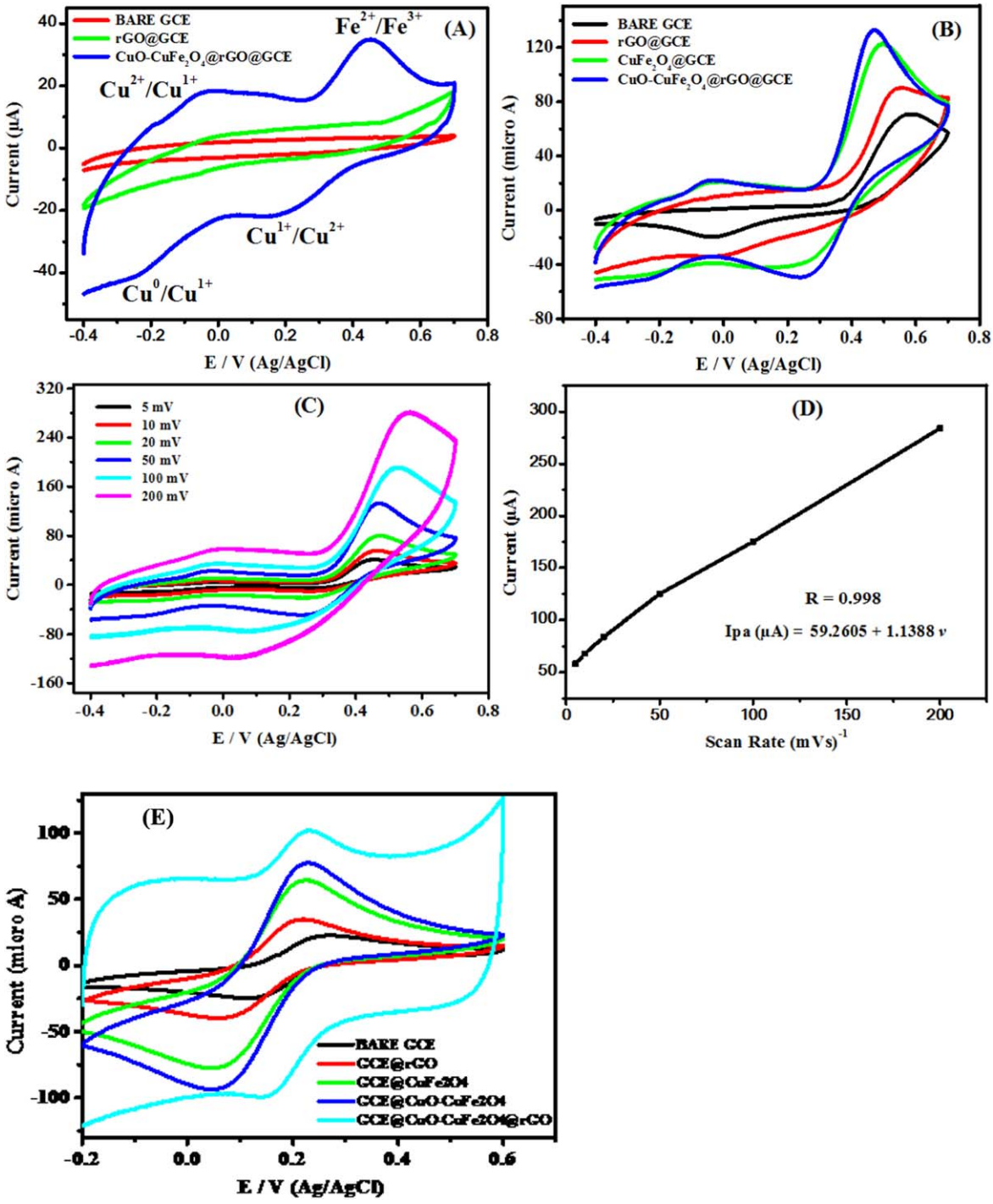

Figure 3. (A) CVs of bare GCE, rGO@GCE and CuO-$CuFe_2O_4$@rGO@GCE modified electrodes in 0.1 M PBS (pH = 7) and (B) with 1.5 mM Paracetamol at scan rate of 50 mVs^{-1}; (C) CVs of different scan rate (2, 10, 20, 50, 100 and 200 mVs^{-1}) in 0.1 M PBS (pH = 7) and (D) Corresponding plot of oxidation current (μA) Vs scan rate (mVs^{-1}) (E) CVs of bare GCE/rGO, GCE/$CuFe_2O_4$, and GCE/CuO-$CuFe_2O_4$ modified electrodes in 10 mM Potassium ferrocyanide $K_3[Fe(CN)_6]$ in 0.1 M KCl solution and compare them with GCE and GCE/CuO-$CuFe_2O_4$@rGO modified electrodes.

oriented along the [002] direction, as expected for rGO sheets. The remaining peaks at $2\theta = 32.5°$, 35.5°, 38.6°, 48.9°, 61.8° and 68.09° correspond to the (110), (−111), (111), (−202) and (220) crystalline planes of CuO NPs, which were perfectly matched with the monoclinic CuO standard pattern (JCPDS file no. 04-0836).[57] This result indicates that the CuO material in the composite is polycrystalline in nature. The observed sharp diffraction peaks confirm the crystallization of the CuO-$CuFe_2O_4$@rGO nanocomposite with good crystallinity of all components of the prepared nanocomposite material. The average crystallite size of the CuO-$CuFe_2O_4$@rGO nanocomposite was calculated using the Scherer equation given by:

$$D = (K\lambda)/(\beta \cos \theta) \quad [1]$$

Where, *D*, *K*, λ, β and θ are the crystallite size, Scherer constant (0.94), X-ray wavelength (1.5406 Å), FWHM (radians) and the angle of diffraction. The calculated average crystallite size was 35.45 nm.

The surface morphology was examined with FE-SEM and HR-TEM characterization techniques. Figure 2A illustrates folded monolayer thin paper like sheet structure. This sheet structure

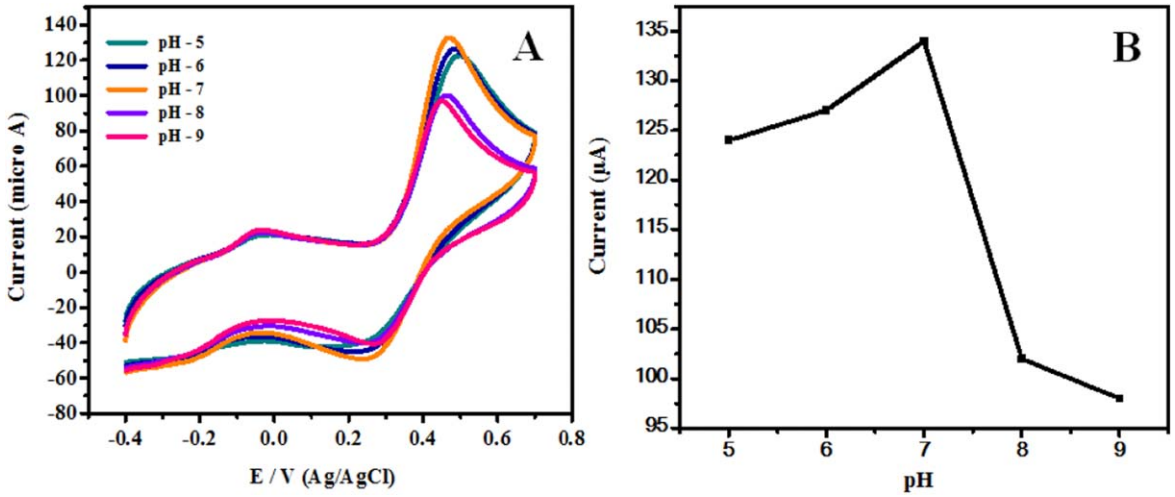

Figure 4. (A) Cyclic voltammograms of CuO-CuFe2O4@rGO@GCE in 0.1 M of PBS and 1.5 mM Paracetamol at different pH values of (5, 6, 7, 8, 9), (B) Relation between oxidation current (Ipa) and pH of supporting electrolyte solution.

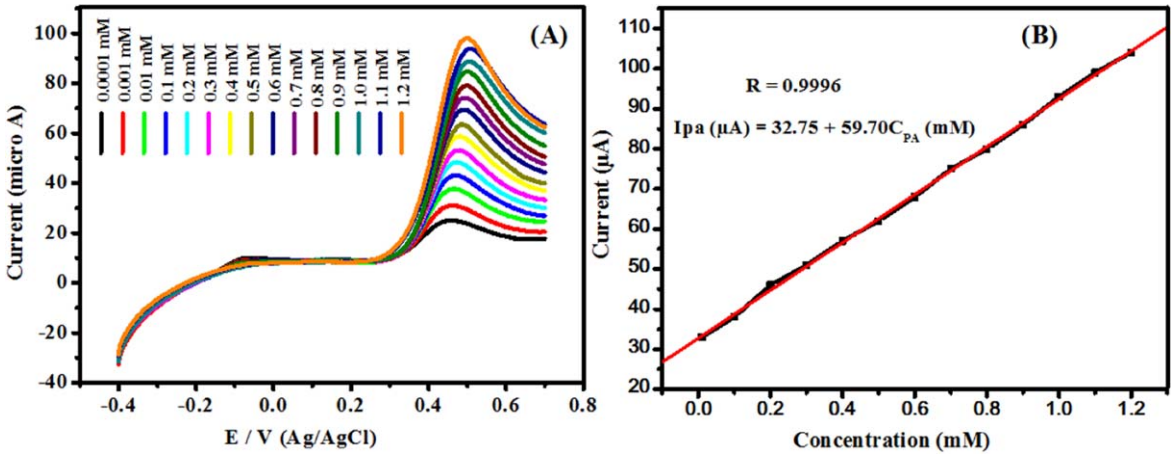

Figure 5. (A) LSVs of CuO-$CuFe_2O_4$@rGO@GCE in various PA concentrations ranging from (0.01, 0.1, 0.2, 0.3, 0.4, 0.5, 0.6, 0.7, 0.8, 0.9, 1.0, 1.1 and 1.2) mM in 0.1 M PBS (pH = 7) and at a scan rate of 50 mVs^{-1}, (B) Relative calibration curve of oxidation current (μA) and concentrations of PA (mM).

Table I. The determination of active surface area for GCE, GCE/rGO, GCE/CuO-$CuFe_2O_4$, and GCE/ CuO-$CuFe_2O_4$@rGO modified electrodes.

Electrodes	Surface area	Unit
BARE GCE	0.014948	cm^2
GCE@RGO	0.022465	cm^2
GCE@$CuFe_2O_4$	0.040321	cm^2
GCE@CuO-$CuFe_2O_4$	0.047838	cm^2
GCE/CuO-$CuFe_2O_4$@rGO	**0.061531**	**cm^2**

Increasing surface area

confirms that the graphite carbon flakes were completely reduced into graphene. These graphene sheet structures afford large support for the attachment and deposition of CuO-$CuFe_2O_4$ nanoparticles. Figures 2B and 2C represent spherical morphology with little agglomeration of highly loaded and uniformly dispersed CuO-$CuFe_2O_4$ nanoparticles over the surface of thin rGO sheets. This proves that rGO sheets not only provide bed but also good anchoring sites for CuO-$CuFe_2O_4$ nanoparticles. As a result, the electrical conductivity of CuO-$CuFe_2O_4$@rGO nanocomposite was improved which in turn increases the electro-activity towards the electro-oxidation of paracetamol. The aforementioned surface texture of CuO-$CuFe_2O_4$@rGO composite material was further

Table II. Electrochemical performance of CuO-$CuFe_2O_4$@rGO sensor compared with reported literatures.

Sr no.	Modified electrode	Oxidation potential (V)	Linear range (μM)	LOD (μM)	Sensitivity $\mu A.mM^{-1}.cm^{-2}$	References
1	SPCE/APTES/nano MIPs	0.05 V	100 to 1000	50.0	6.18	1
2	NiO/GCE	0.35 V	7.5 to 3000	0.23	91.0	4
3	N-CeO_2@rGO	0.57 V	0.05 to 0.600	0.0098	268	61
4	TiO_2/PB/AuNPs/CMK3/Nafion/GE	0.7 V	10 to 52	0.210	11.56	62
5	PSAF-MCPE	0.31 V	10 to 100	4.7	—	63
6	NiONPs-CB-DHP/GCE	0.61 V	3.0 to 47.8	0.12	4.042	64
7	GO-XDA-Mn_2O_3/GCE	0.527 V	01 to 1000	0.056	527.04	23
8	Pd@α-MnO_2/G	0.43 V	0.1 to 375	0.059	0.0854 $\mu A.\mu M^{-1}$	65
9	PPy.SDS carbon fibre	0.59 V	50 to 500	33.8	—	66
10	Gr/CNF-AgNPs	0.645 V	01 to 340	0.019	0.012 $\mu A\mu M^{-1}$	67
11	ILC-CPE	0.63 V	00 to 120	2.8	0.0123 $\mu A\mu M^{-1}$	68
12	TX-100/MgO/MCP	0.35 V	10 to 100	6.2	—	69
13	CuO-$CuFe_2O_4$@rGO@GCE	0.47 V	10 to 1200	7.0	970.26	Present work

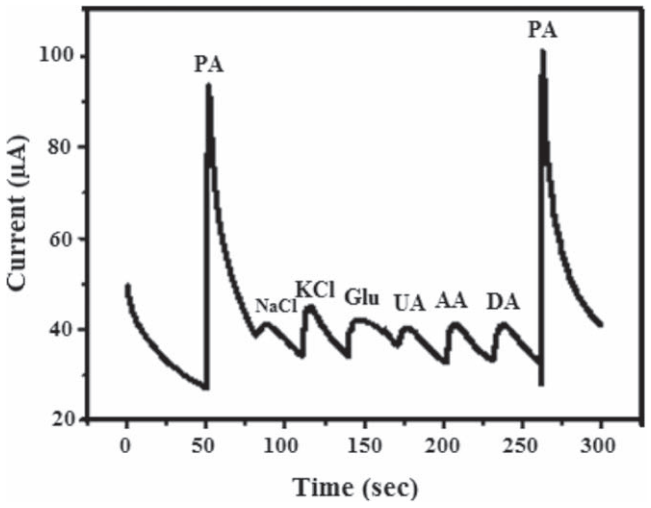

Figure 6. Amperometric current-time (i–t) response measured for 1 mM PA and various interfering species (NaCl, KCl, Glu, AA, DA and UA) 1.0 mM each at CuO-$CuFe_2O_4$@rGO@GCE in 0.1 M PBS (pH = 7) at 0.47 V.

confirmed by HR-TEM images. It can be seen that rGO nanosheets exhibited folded ultrathin structure with few wrinkles (Fig. 2D).[58] Additionally, it was confirmed that CuO-$CuFe_2O_4$ has spherical morphology with uniform distribution on the surface of rGO sheets (Figs. 2E–2G). The uniform diffraction rings in the selected area electron diffraction (SAED) patterns (Fig. 2H) correspond to the metal oxide phases, indicating that these oxides are polycrystalline in nature, whereas the bright spots are indicative of highly oriented crystal planes, and are associated reflections from the rGO sheets; these results are consistent with the powder XRD patterns.

Analysis of electrochemical active surface area (ECSA).— (Figure S2) illustrates the cyclic voltamograms of bare GCE and CuO-$CuFe_2O_4$@rGO modified electrodes in 10 mM potassium ferrocyanide $K_3[Fe(CN)_6]$ in 0.1 M KCl solution at a scan rate of 50 mVs^{-1}. As can be seen from (Fig. S2), it is clear that CuO-$CuFe_2O_4$@rGO modified electrode exhibited high redox current with well developed redox peaks compared to the bare GC electrode. This indicates that the CuO-$CuFe_2O_4$@rGO electrode active surface area has been greatly improved. The active surface area was calculated by using Randles-Sevcik equation given by:

$$Ip = 2.69 \times 10^5 . n^{3/2} . D^{1/2} . A . v^{1/2} . C \qquad [2]$$

Where, *Ip, n, D, A, v* and *C* are peak current (μA), no. of electrons involved in the redox reaction ($n = 1$), diffusion coefficient (7.6×10^{-6} cm^2 s^{-1}), area (cm^2), scan rate (0.05 V s^{-1}) and concentration

Table III. The determination of paracetamol in real sample application.

Sample	PA Added (mM)	Detected (mM)	Recovery %
1	1.0	0.97	97
2	2.0	1.93	96.5
3	3.0	2.94	98
4	4.0	3.90	97.5

(10 mM), respectively. The results of the calculations (Table I) clearly indicate the superiority of the synthesized nanocomposite in terms of the enhancement of the active surface area.

Electrochemical activity of CuO-$CuFe_2O_4$@rGO nanocomposite.— The electrochemical activity of the GCE, rGO@GCE, $CuFe_2O_4$@rGO and CuO-$CuFe_2O_4$@rGO designed electrodes were performed in the absence (Fig. 3A) and presence of 1.5 mM paracetamol (Fig. 3B) in 0.1 M PBS (pH =7.0) at 50 mVs^{-1}. It is clear (Fig. 3A) that no distinct redox peaks were exhibited by the bare G'CE, rGO@GCE in PBS solution, whereas well developed characteristic redox peaks were observed for the CuO-$CuFe_2O_4$@rGO modified electrode. Among these, the anodic peaks observed at $E_{pa} = -0.25$ V and $E_{pa} = 0.14$ V are attributed to the oxidation of Cu^0 to Cu^{1+} and Cu^{1+} to Cu^{2+} while the cathodic peak noticed $E_{pc} = -0.08$ V corresponds to the reduction of Cu^{2+} to Cu^{1+}. On the other hand, the anodic peak at $E_{pa} = 0.46$ V was ascribed to oxidation of Fe^{2+}/Fe^{3+} redox pair.[59,60] However, upon the addition of 1.5 mM PA solution, GCE and rGO@GCE shows significantly lower oxidation current with irreversible oxidation peaks at high potential of $E_{pa} = 0.59$ and 0.55 V, respectively. Besides, $CuFe_2O_4$@GCE showed a couple of reversible redox peaks with slight increment in current at anodic and cathodic peak potentials of $E_{pa} = 0.50$, $E_{pc} = 0.27$ V, respectively. Nevertheless, CuO-$CuFe_2O_4$@rGO modified electrode displayed a pair of well-developed oxidation and reduction peaks along with significant enhancement in redox current with the decrease in the over potential. The redox peaks are observed at $E_{pa} = 0.47$ and $E_{pc} = 0.24$ V, respectively. The redox potential was shifted negatively as compared to the bare GCE, rGO and $CuFe_2O_4$ modified electrodes. The active surface area for GCE, GCE/rGO, GCE/CuO-$CuFe_2O_4$, and GCE/CuO-$CuFe_2O_4$@rGO modified electrodes have calculated in (Table I). This is because of faster electron transport from CuO-$CuFe_2O_4$ to analyte molecules over a large matrix of rGO nanosheets. This evidence proves that CuO-$CuFe_2O_4$@rGO is highly electro-active material compared to the bare GCE, rGO and $CuFe_2O_4$ nanoparticles. The above outcome was greatly attributed

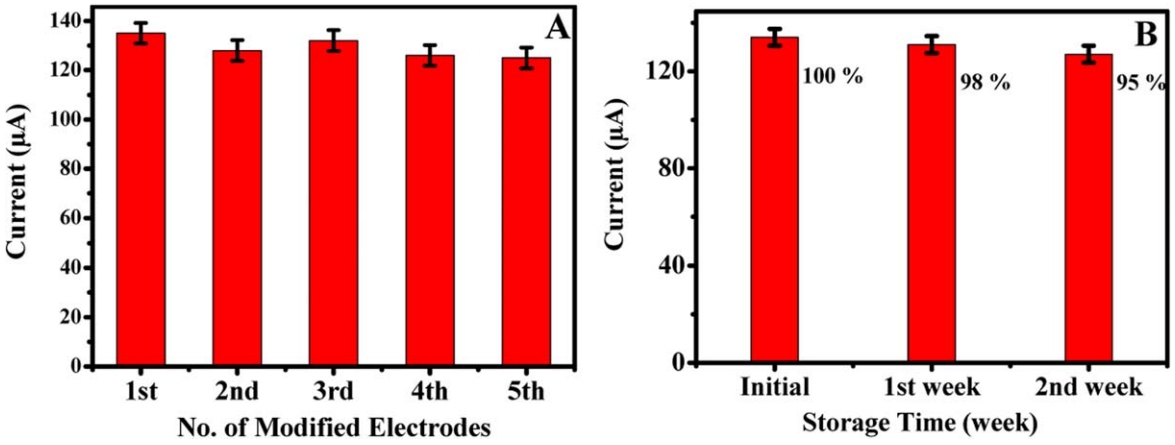

Figure 7. Bar diagrams of (A) Reproducibility (relation between oxidation current and modified electrodes) and (B) Stability study of CuO-$CuFe_2O_4$@rGO@GCE for 1.5 mM PA under the same experimental conditions.

to the synergistic effect as well as the hetero metal ions such as Cu^{2+} and Fe^{3+} present in mixed oxidation state in an electro-catalyst which boosts an electron transfer and lowers the over potential due to the enhanced active surface area of the catalytic material towards paracetamol oxidation reaction.[4,61,62]

Scan rate effect.—Figure 3C shows the cyclic voltammograms at different scan rates (5, 10, 20, 50, 100 and 200 mVs^{-1}). As can be seen from (Figs. 3C and 3D), the oxidation current increases linearly with the sweep rate. The linear regression relation is given as I_{pa} (μA) = 59.2605 + 1.1388 v with regression coefficient R = 0.998. In addition, (Fig. S1), shows the relation between log (I_a) vs log (v). This plot revealed a linear relation of the form log (I_a) = 1.27 + 0.506 log (v) with regression coefficient R = 0.9988. The slope of the plot was found to be 0.5 which is the standard reported value for the controlled diffusion process. Henceforth, according to the previous literature, the electro-oxidation reaction of paracetamol is a diffusion-controlled process.[4,63]

Optimization of pH.—An oxidation reaction of paracetamol is dependent on pH of supporting electrolyte solution. Therefore, it is necessary to examine the effect of pH on the oxidation of paracetamol. Figure 4A shows the cyclic voltammograms of oxidation peak current for 1.5 mM paracetamol in 0.1 M PBS solution at various pH values. Figure 4B clearly demonstrates that the rate of oxidation reaction enhanced with increasing the pH value of the solution. As a result, the anodic peak current increases with the increase of pH up to 7, and then decreases rapidly at higher pH values. This result indicates that the rate of oxidation of paracetamol was reduced at higher alkaline pH values.[21] These results indicate that equal numbers of H^+ and e^{-1} were transferred during the paracetamol oxidation reaction.[33,34] Thus, 0.1 M phosphate buffer solution (pH = 7) was selected as a supporting medium for further analysis of paracetamol.

Concentration effect and calibration curve.—Figure 5A, demonstrates linear sweep voltammograms (LSV) of CuO-$CuFe_2O_4$@rGO nanocomposite at different paracetamol concentrations ranging from 0.01 mM to 1.2 mM in 0.1 M of PBS (pH = 7). It was observed that the peak current increases progressively as a function of concentration. Figure 5B displays a calibration curve for the oxidation current against paracetamol concentrations. The calibration curve showed a good linearity in the dynamic range from 0.01 to 1.2 mM in accordance with the relation I_{pa} (μA) = 32.75 + 59.70C_{PA} (mM) and regression coefficient of R = 0.9996. The modified electrode exhibited excellent sensitivity of 970.26 $\mu A.mM^{-1}.cm^{-2}$. The calculated values of LOD and LOQ were found to be 0.007 mM and 0.025 mM, respectively.

The electrochemical performance of CuO-$CuFe_2O_4$@rGO towards paracetamol electro-oxidation is compared to reported results for other electrode materials in (Table II). The superiority of the modified electrochemical sensor performance in this work with higher sensitivity, low detection limit, and a wide linear range compared to other electrode materials is clear. The superior performance of the electrode material in this study is credited to the large active surface area of the nanocomposite and the combined synergistic effect of rGO, CuO, $CuFe_2O_4$ NPs.

Selectivity study of the sensor.—The selectivity is an important analytical feature of an electro-chemical sensor. It is the potential of the sensor to distinguish electro-active species with comparable structural properties to sample molecule. An interfering species including glucose (Glu), ascorbic acid (AA), dopamine (DA), uric acid (UA), KCl and NaCl were used for the selectivity study. Among these, dopamine (DA) is similar to 4-acetaminophen (PA) while glucose, ascorbic acid, uric acid, NaCl and KCl are other co-existing species in the body. The interfering species showed negligible current in contrast to 4-acetaminophen. It was due to the varied oxidation potentials of interfering species as compared to paracetamol (0.47 V). Evidently, the CuO-$CuFe_2O_4$@rGO/GCE sensor furnishes excellent discrimination property and selectivity towards paracetamol oxidation (Fig. 6). The higher selectivity is attributed to the spherical morphology, mixed oxidation states of metal (Cu^{2+} and Fe^{3+}) ions and the high active surface area of the synthesized nanocomposite material.

Reproducibility and stability.—The reproducibility of CuO-$CuFe_2O_4$@rGO modified electrode was evaluated through Measuring the current response of five electrodes designed by the same experimental procedure and the relative standard deviation (RSD %) was calculate to about 3.26% for 1.5 mM concentration of Paracetamol (Figs. S3A and 7A). The long-term stability of the fabricated electrode was studied by an interval of 7 d while preserved at 4 °C in a refrigerator. The current response was found to be stable upto 95% of its original current measured after two weeks (14 d) under the same experimental conditions (Figs. S3B and 7B). The above results signify that the fabricated CuO-$CuFe_2O_4$@rGO/GCE sensor demonstrates excellent stability and reproducibility towards the electro-oxidation of Paracetamol drug.

Real sample analysis.—The performance of the CuO-$CuFe_2O_4$@rGO modified sensor for the detection of paracetamol in real samples was studied by using a standard addition method to urine samples. Different concentrations of the commercially available paracetamol tablets (PCM-500) were added to urine samples and the content of PA and its % Recovery are presented in (Table III). It was observed that the method is reliable upto 97.25%. These results recommended that the constructed PA sensor can be successfully applied for the detection of paracetamol drug in routine application.

Conclusions

This study describes the efficient hydrothermal synthesis of the CuO-$CuFe_2O_4$@rGO nanocomposite. Here, a single aqueous NaOH solution functions as a reducing & sol-gel reagent that generates CuO & $CuFe_2O_4$ NPs in the absence of hazardous reducing chemicals and polymer solution. The structural and morphological information were analysed by using XRD, FE-SEM and HR-TEM characterization techniques. The synthesized nanocomposite displayed highly dispersed spherical particles deposited over of rGO nanosheets support. From XRD analysis, the crystallite size of the CuO-$CuFe_2O_4$ NPs was found to be 35.5 nm. Owing to the large active surface area and high conductivity of CuO-$CuFe_2O_4$@rGO nanocomposite material, the catalytic performance of nanocomposite was greatly improved. As a result, the fabricated electro-chemical sensor exhibited excellent sensitivity, selectivity, rapid response, higher stability and reproducibility along with good linearity and low detection limit. Finally, the above improvement in the sensor properties is attributed to the good morphology of nanocomposite as well as the combined synergistic effect of rGO, CuO and $CuFe_2O_4$ NPs.

Acknowledgments

The author appreciatively thanks to the KET'S V. G. Vaze College (Autonomous) and research laboratory staff for their kind support. Authors are also grateful to SAIF, IIT Bombay for SEM and TEM characterization techniques. Moreover, thanks to Department of MEMS, IIT Bombay for XRD analysis technique.

ORCID

Trimurti L. Lambat https://orcid.org/0000-0002-4039-4097
Suresh S. Shendage https://orcid.org/0000-0002-9530-8109

References

1. K. Alanazi et al., *Sensors Actuators B*, **329**, 129128 (2020).
2. A. Pollap, K. Baran, N. Kuszewska, and J. Kochana, *J. Electroanalytical Chemistry*, **878**, 114574 (2020).
3. M. Burç, S. Köytepe, S. T. Duran, N. Ayhan, B. Ş. Aksoy, and T. Seçkin, *Measurement*, **151**, 107103 (2019).

4. K. Annadurai, V. Sudha, G. Murugadoss, and R. Thangamuthu, *J. Alloys and Compounds*, **852**, 156911 (2021).
5. V. A. Kumary, J. Divya, T. E. M. Nancy, and K. Sreevalsan, *Int. J. Electrochem. Sci.*, **8**, 6610 (2013).
6. L. Yang, B. Zhang, B. Xu, F. Zhao, and B. Zeng, *Talanta*, **224**, 121845 (2021).
7. D. L. Oldair, *Quim. Nova*, **32**, 1755 (2009).
8. P. Zhou, M. She, P. Liu, S. Zhang, and J. Li, *Sensors Actuators B*, **318**, 128258 (2020).
9. K. Sirajuddin, R. Abdul, A. Shah, M. I. Bhanger, A. Niaz, and S. Mahesar, *Spectrochim. Acta A*, **68**, 747 (2007).
10. M. E. C. Peiro, D. Bose, M. F. Rubert, and J. E. Romero, *J. Chromatogr. B*, **839**, 95 (2006).
11. A. Goyal and S. Jain, *Acta Pharm. Sci.*, **49**, 147 (2007).
12. C. S. Wesley, P. F. Pereira, M. C. Marra, D. T. Gimenes, R. R. Cunha, R. A. B. da Silva, R. A. A. Munoz, and E. M. Richter, *Electroanalysis*, **23**, 2764 (2011).
13. G. Burgos, F. Auffret, and J. L. Burgos, *Anal. Chim. Acta*, **343**, 125 (1997).
14. T. S. S. K. Naik, M. M. Mwaurah, and B. E. K. Swamy, *J. Electroanal. Chem.*, **834**, 71 (2019).
15. K. Chetankumar, B. E. K. Swamy, and S. C. Sharma, *Microchem. J.*, **156**, 104979 (2020).
16. S. M. Azab, *J. Electroanalytical Chemistry*, **840**, 319 (2019).
17. K. Chetankumar, B. E. K. Swamy, and S. C. Sharma, *J. Electroanal. Chem.*, **849**, 113365 (2019).
18. K. Chetankumar, B. E. K. Swamy, and T. S. S. K. Naik, *Chem. Data Collect.*, **28**, 100392 (2020).
19. B. Avinash, C. R. Ravikumar, M. R. Anil Kumar, H. P. Nagaswarupa, M. S. Santosh, A. S. Bhatt, and D. Kuznetsov, *Journal of Physics and Chemistry of Solids*, **134**, 193 (2019).
20. K. G. Manjunatha, B. E. Kumara Swamy, H. D. Madhuchandra, and K. A. Vishnumurthy, *Chemical Data Collections*, **31**, 100604 (2021).
21. A. Mao, H. Li, D. Jin, L. Yu, and X. Hu, *Talanta*, **44**, 252 (2015).
22. M. Baccarina, F. A. Santos, F. C. Vicentini, V. Zucolotto, B. C. Janegitz, and O. F. Filho, *J. Electroanalytical Chemistry*, **799**, 436 (2017).
23. A. Ejaz and S. Jeon, *Electrochim. Acta*, **245**, 742 (2017).
24. N. F. Atta, Y. M. Ahmed, and A. Galal, *Journal of Electroanalytical Chemistry*, **828**, 11 (2018).
25. J. V. H. Ramos, F. D. M. Morawski, T. M. H. Costa, S. L. P. Dias, E. V. Benvenutti, E. W. D. Menezes, and L. T. Arenas, *Microporous Mesoporous Mater.*, **217**, 109 (2015).
26. M. Baccarin, F. A. Santos, F. C. Vicentini, V. Zucolotto, B. C. Janegitz, and O. F. Filhoa, *J. Electroanalytical Chemistry*, **799**, 436 (2017).
27. Y. E. L. Bouabi, A. Farahi, N. Labjar, S. E. Hajjaji, M. Bakasse, and M. A. E. Mhammedi, *Materials Science & Engineering C* (2015).
28. S. Shahrokhian and R. S. Saberi, *Inter. J. Electrochemistry*.
29. T. S. S. Kumar Naik, B. E. K. Swamy, P. C. Ramamurthy, and K. Chetankumar, *Materials Science for Energy Technologies*, **3**, 626 (2020).
30. Y. Dai, X. Li, X. Lu, and X. Kan, *Microchim. Acta* (2016).
31. J. Luo, C. Fan, X. Wang, R. Liu, and X. Liu, *Sensors and Actuators B*, **188**, 909 (2013).
32. A. Kader, M. M. Shamsuddin, and A. S. Jeon, *Appl. Surf. Sci.*, **578**, 152090 (2022).
33. N. F. Atta, M. F. E. Kady, and A. Galal, *Sensors Actuators B*, **141**, 566 (2009).
34. J. Li, J. Liu, G. Tan, J. Jiang, S. Peng, M. Deng, D. Qian, Y. Feng, and Y. Liu, *Biosens. Bioelectron.*, **54**, 468 (2014).
35. L. Wang, Y. Yang, H. Liang, N. Wu, X. Peng, L. Wang, and Y. Song, *J. Hazardous Materials*, **409**, 124528 (2021).
36. Q. Li, D. Chen, J. Miao, S. Lin, Z. Yu, D. Cui, Z. Yang, and X. Chen, *Sensors & Actuators: B. Chemical*, **326**, 128952 (2021).
37. A. Umar, A. A. Ibrahim, U. T. Nakate, H. Albargi, M. A. Alsaiari, F. Ahmed, F. A. Alharthi, A. A. Alghamdi, and N. A. Zaqri, *Chem. Phys. Lett.*, **763**, 138204 (2021).
38. B. R. Wang, R. Z. Wang, Y. J. Bai, L. Y. Liu, and Q. L. Jiang, *J Alloys and Compounds*, **877**, 160277 (2021).
39. Z. Rafiee, H. Roshan, and M. H. Sheikhi, *Ceram. Int.*, **47**(4), 5311 (2021).
40. H. Yang, G. Cao, Y. Huang, Y. Lin, F. Zheng, L. Lin, F. Liu, and S. Li, *Journal of Pharmaceutical Analysis*, **12**, 436 (2022).
41. D. S. Patil, N. P. Shetti, D. S. Nayak, and R. S. Revankar, *Mater. Today Proc.*, **18**, 1124 (2019).
42. K. M. Navada, G. K. Nagaraja, J. N. D'Souza, S. Kouser, C. R. Ravikumar, and D. J. Manasa, *Ceram. Int.*, **47**, 33651 (2021).
43. K. P. O. Mahesh, I. Shown, L. C. Chen, K. H. Chen, and Y. Tai, *Appl. Surf. Sci.*, **427** (Part B), 387 (2018).
44. Y. Liu, W. Zhao, X. Li, J. Liu, Y. Han, J. Wu, X. Zhang, and Y. Xu, *Appl. Surf. Sci.*, **512**, 145710 (2020).
45. S. F. Chong, K. A. Razak, N. M. Nor, N. S. Ridhuan, and N. D. Zakaria, *Mater. Today Proc.*, **17**, 1189 (2019).
46. Z. Yang, X. Zheng, and J. Zheng, *J. Alloys and Compounds*, **709**, 581 (2017).
47. G. Mathew, P. Dey, R. Das, S. D. Chowdhury, M. P. Das, P. Veluswamy, B. Neppoliana, and J. Das, *Biosens. Bioelectron.*, **115**, 53 (2018).
48. J. Liu, L. Sun, G. Li, H. Jue, and Q. He, *Mater. Res. Bull.*, **133**, 111050 (2021).
49. Z. Yu, H. Li, J. Lu, X. Zhang, N. Liu, and X. Zhang, *Electrochim. Acta*, **185**, 264 (2015).
50. D. C. Marcano, D. V. Kosynkin, J. M. Berlin, A. Sinitskii, Z. Sun, A. Slesarev, L. B. Alemany, W. Lu, and J. M. Tour, *ACS Nano*, **4**, 4806 (2010).
51. J. Song, X. Wang, and C. T. Chang, *J. Nanomater.*, **2014**, 6 (2014).
52. J. Zheng, Z. Lin, W. Liu, L. Wang, S. Zhao, H. Yang, and L. Zhang, *J. Mater. Chem. B*, **2**, 6207 (2014).
53. B. R. Vergis, R. H. Krishna, N. Kottam, B. M. Nagabhushana, R. Sharath, and B. Darukaprasad, *J. Nanostructure in Chemistry*, **8**, 1 (2018).
54. Y. Tang, K. Shih, C. Liu, and C. Liao, *RSC Adv.*, **6**, 28579 (2016).
55. M. A. Haija, G. Basina, F. Banat, and A. I. Ayesh, *Materials Science-Poland*, **37** (2019).
56. F. Liu, Q. Xu, W. Huang, Z. Zhang, G. Xiang, C. Zhang, C. Liang, H. Lian, and J. Peng, *Electrochim. Acta*, **295**, 615 (2019).
57. X. Wang, E. Liu, and X. Zhang, *Electrochim. Acta*, **130**, 253 (2014).
58. X. Kang, J. Wang, H. Wu, J. Liu, I. A. Aksay, and Y. Lin, *Talanta*, **81**, 754 (2010).
59. Z. Zhang and P. Wang, "Highly stable copper oxide composite as an effective photocathode for water splitting via a facile electrochemical synthesis strategy." *J. Mater. Chem.*, **22**, 2456 (2012).
60. M. H. Bridge, E. Williams, M. E. G. Lyons, K. F. Tipton, and W. Linert, "Electrochemical investigation into the redox activity of Fe(II)/Fe(III) in the presence of nicotine and possible relations to neurodegenerative diseases." *Biochim. Biophys. Acta*, **1690**, 77 (2004).
61. S. K. Ponnaiah, P. Prakash, and B. Vellaichamy, *Ultrason, Sonochem*, **44**, 196 (2018).
62. A. Pollap, K. Baran, N. Kuszewska, and J. Kochana, *J. Electroanalytical Chemistry* (2020).
63. K. Chetankumar, B. E. K. Swamy, and S. C. Sharma, *Microchemical Journal-B*, **160**, 105729 (2021).
64. P. B. Deroco, F. C. Vicentini, and O. F. Filho, *Electroanalysis*, **27**, 2214 (2015).
65. A. K. Mohiuddin, M. S. Ahmed, and S. Jeon, *Appl. Surf. Sci.*, **578**, 152090 (2022).
66. S. Sriprasertsuk, S. C. Mathias, J. R. Varcoe, and C. Crean, *J. Electroanalytical Chemistry*, **897**, 115608 (2021).
67. A. S. Santhosh, S. Sandeep, D. J. Bound, S. Nandini, S. Nalini, G. S. Suresh, N. Kumara Swamy, J. R. Rajabathar, and A. Selvaraj, *Surfaces and Interfaces*, **26**, 101377 (2021).
68. R. Mangaiyarkarasi, S. Premlatha, R. Khan, R. Pratibha, and S. Umadevi, *J. Molecular Liquids*, **319**, 114255 (2020).
69. K. G. Manjunatha, B. E. Kumara Swamy, H. D. Madhuchandra, K. J. Gururaj, and K. A. Vishnumurthy, *Sensors International*, **2**, 100127 (2021).